

Correlations in Nonequilibrium Steady States of Random Halves Models

Kevin K. Lin* Lai-Sang Young†

Courant Institute of Mathematical Sciences
New York University

February 23, 2007

Abstract

We present the results of a detailed study of energy correlations at steady state for a 1-D model of coupled energy and matter transport. Our aim is to discover — via theoretical arguments, conjectures, and numerical simulations — how spatial covariances scale with system size, their relations to local thermodynamic quantities, and the randomizing effects of heat baths. Among our findings are that short-range covariances respond quadratically to local temperature gradients, and long-range covariances decay linearly with macroscopic distance. These findings are consistent with exact results for the simple exclusion and KMP models.

Contents

Introduction	2
1 The Random Halves Model	3
1.1 Model Description and Physical Interpretation	3
1.2 Invariant Measures at Equilibrium	5
1.3 Macroscopic Equations of Nonequilibrium Steady States	6
2 Global Fluctuations and Pair Correlations	7
2.1 Scaling of Total-Energy Variance	7
2.2 Pair Covariances	9
3 Covariance Structures “at $N = \infty$”	11

*E-mail: klin@cims.nyu.edu . This research was supported by an NSF Postdoctoral Fellowship.

†E-mail: lsy@cims.nyu.edu . This research was supported by a grant from the NSF.

4	Covariances at Microscopic Distances: $\rho_L = \rho_R$	12
4.1	The two middle sites	12
4.2	Quadratic responses to local temperature gradients	14
4.3	Boundary effects	15
5	Covariances at Microscopic Distances: $\rho_L \neq \rho_R$	18
5.1	Responses to local gradients	18
5.2	Far-from-equilibrium corrections	20
5.3	Nearest-neighbor covariances in long chains	21
6	Long-range Covariances	21
6.1	Renormalizability and the function $\mathcal{C}_2(x, y)$	21
6.2	An approximate formula	24
	Conclusions and Remarks	25
	Appendices	26

Introduction

Transport processes, such as heat flow through a conducting medium in contact with unequal heat reservoirs, are intrinsically nonequilibrium phenomena because of the presence of nonzero currents [5, 17]. A central problem in nonequilibrium statistical physics is to explain how such large-scale, macroscopic processes arise from complex microscopic interactions. The most basic questions are perhaps those of mean profiles of quantities of physical interest and their responses to external forces. Nonequilibrium steady states, on the other hand, are well known to be characterized by large fluctuations, and among the simplest measures of fluctuations are temporal and spatial correlations.

In this paper, we present a systematic study of spatial correlations at steady state for a class of 1-D stochastic models called Random Halves Models. A detailed description of this class of models is given in Sect. 1.1. Very briefly, a linear chain of open cells is connected to two unequal heat baths, which inject into the chain tracer particles at characteristic rates and energies. Energy storage devices are systematically placed throughout the chain to mark local energy levels. Their contents are redistributed by the tracer particles as they move through the chain. These models were introduced in [9] as stochastic idealizations of certain mechanical models [16, 18].

Our study is based on a combination of analytic arguments and numerical simulations. We believe random halves models are excellent candidates for this method of investigation for two reasons. First, their dynamics are richer and more complex than rigorously-understood models such as the simple exclusion [6] and KMP models [13], as random halves models have two transported quantities (energy and matter) and highly nonlinear interactions involving two different time scales. These features make a purely analytical study more difficult. Second, all of the forces acting on this system are clearly identified. This is seldom the case in more realistic physical models.

Our main results can be summarized as follows. Given boundary conditions, *i.e.*, the temperature and injection rate of each bath, we let S_i denote the stored energy at the i th site, and $\text{Cov}_N(S_i, S_j)$ the covariance of S_i and S_j in a chain of length N . Our first finding is $\text{Cov}_N(S_i, S_j) \sim \frac{1}{N}$ for $i \neq j$, which leads us to consider the following two functions describing the covariances of stored energies at microscopic and macroscopic distances:

$$\begin{aligned} \mathcal{C}(x) &= \lim_{N \rightarrow \infty} N \cdot \text{Cov}_N(S_{[xN]}, S_{[xN]+1}), & x \in (0, 1); \\ \mathcal{C}_2(x, y) &= \lim_{N \rightarrow \infty} N \cdot \text{Cov}_N(S_{[xN]}, S_{[yN]}), & x, y \in (0, 1), \quad x \neq y. \end{aligned}$$

We show that $\mathcal{C}(x)$ has the form

$$\mathcal{C}(x) \approx \hat{\varphi}^{bc}(x) \cdot A(\kappa(x)) \cdot T'(x)^2 \tag{1}$$

where the right side is to be interpreted as follows: $\hat{\varphi}^{bc}(x)$ is a measure of effective distance to the baths, a rough approximation of which is $\hat{\varphi}^{bc}(x) \approx 4x(1-x)$; $T(x)$ is local temperature, and $T'(x)$ is temperature gradient; $\kappa(x)$ is local particle density, and $A(\kappa) \rightarrow 0$ as $\kappa \rightarrow \infty$. Note the quadratic dependence on the local temperature gradient. For long-range covariances, we find that for fixed x , the function $y \mapsto \mathcal{C}_2(x, y)$ is continuous but not differentiable at $y = x$, decreasing roughly linearly as $|y - x|$ increases.

Our numerical results are consistent with exact analytic results on the simple exclusion and KMP models [6, 7, 20, 3]. We extend the existing picture to a setting of coupled energy and matter transport, with features not present in these two previously studied models. For example, we show that energy covariances at microscopic distances respond quadratically to local temperature gradients (which vary along the chain; see [9]). There is a second transported quantity, namely matter in the form of particles, and energy covariances are shown to be inversely related to local particle density. Throughout the paper, we provide cross-checking numerical evidence for the phenomena we identify, and venture to give a physical interpretation whenever we can. See [1, 2, 11, 14, 15] for other relevant works on this topic.

While most of the results presented here are specific to 1-D, they also serve as a basis for direct comparisons with higher dimensions. A corresponding analysis of random halves models in 2 and 3-D is underway. The results will be reported in a separate paper.

Note on simulations. All of our numerical results are obtained via direct simulation. That is, our computer programs faithfully implement the dynamics of the random halves model described in Sect. 1.1, and expectation values with respect to the invariant measures are computed as time averages over long trajectories. Some relevant numerical issues are discussed in Appendix A.

1 The Random Halves Model

1.1 Model Description and Physical Interpretation

A class of models of nonequilibrium phenomena is introduced in [9]. In each model, there is a homogeneous conducting medium represented by a linear chain of N identical “cells” with stochastic

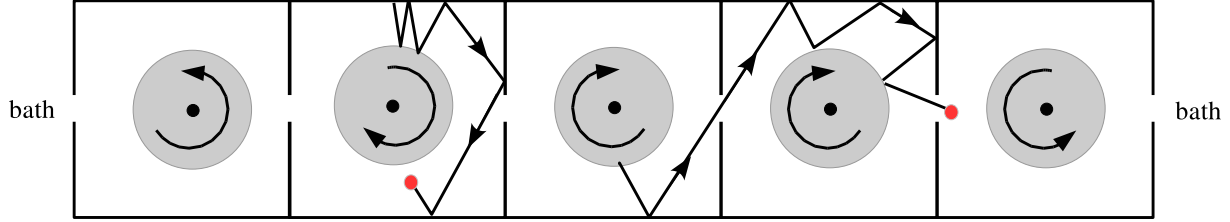


Figure 1: The rotating disc model. The “random halves” model studied in this paper is a stochastic version of this model.

heat baths coupled to the ends of the chain. Within each cell, there is a *stored energy* which characterizes the “temperature” at that location. Matter (in the form of tracer particles) and energy (in the form of tracer kinetic energy) are injected into the system by the heat baths; they are eventually absorbed by the heat baths. Tracer particles interact with the local system at each site, redistributing the stored energies as they move about in the chain; they do not interact directly with each other. This general framework was introduced as an abstraction of the mechanical models in [16, 18]. It encompasses both “Hamiltonian” models with conservative deterministic dynamics (the heat baths being the only sources of randomness), and stochastic models, in which the microscopic dynamics are defined by conservative stochastic rules.

For concreteness, we begin by describing a slightly simplified version of the mechanical models studied in [16, 18]. In this *rotating disc model*, each cell contains a disc nailed down at its center, about which it rotates freely (see Fig. 1). Whenever a tracer collides with a disc, it exchanges kinetic energy with the disc via a deterministic rule, *e.g.* the angular momentum of the disc may be interchanged with the tangential component of the tracer’s momentum. When a tracer collides with a cell wall, it reflects elastically. Here, the stored energy at each site is the rotational energy of the disc.

The random halves model studied in the present paper are stochastic idealizations of mechanical models like the rotating disc model described above. Nonequilibrium energy and particle density profiles of random halves models have been analyzed in [9]. The rest of this section reviews relevant parts of that paper.

Precise description of the Random Halves Model. There are N sites, labeled $1, 2, \dots, N$, with tracers moving through the chain. At each site there is an abstract *energy storage tank*. We let $S_i(t)$ denote the amount of energy in the tank at site i at time t . The microscopic dynamics are defined by the following rules. Fix $\delta > 0$. Each tracer is equipped with two independent exponential clocks. Clock 1, which signals the times of energy exchanges with tanks, rings at rate $\sqrt{e(t)}/\delta$, where e is the kinetic energy of the tracer. Clock 2, which signals the times of site-to-site movements, rings at rate $\sqrt{e(t)}$. Suppose a tracer is at site i and one of its clocks rings. Then instantaneously:

- (i) If Clock 1 rings, the tracer energy e and the stored energy S_i are pooled together and split randomly. That is, the tracer gets $U \cdot (e + S_i)$ units of energy and the tank gets $(1 - U) \cdot (e + S_i)$, where $U \in [0, 1]$ is uniformly distributed and independent of all other random variables.

- (ii) If Clock 2 rings, the tracer leaves site i . It jumps with equal probability to sites $i \pm 1$. A tracer entering site 0 or site $N + 1$ exits the system forever.

All tracers originate from and eventually exit to one of the heat baths. Each heat bath injects tracers with independent, exponentially-distributed energies into the system. The left bath injects tracers with mean energy T_L into site 1 at an exponential rate of ρ_L , and the right bath injects tracers with mean energy T_R into site N at a rate of ρ_R . Tracers in the system are indistinguishable.

Physical interpretation and remarks. It is natural to think of the parameters T_L and T_R as temperatures. This leads us to define the temperature T_i at site i in an N -chain to be $T_i := \mathbb{E}(S_i)$, where the expectation is taken with respect to the invariant measure of the N -chain. The injection rates ρ_L and ρ_R can be rewritten in terms of chemical potentials; we do not pursue this analogy further.

The Hamiltonian model contains a small length parameter which does not appear in the stochastic model, namely a length ℓ which measures the size of the cell. In the stochastic model, we set $\ell = 1$. It is useful to keep this in mind in dimensional analysis.

There are two time scales in our system, one associated with the local dynamics at each site and the other the movement of tracers along the chain. The ratio of these two time scales is δ . For example, $\delta \ll 1$ means that on average, tracer-tank energy exchanges occur much more frequently than site-to-site movements of tracers. Steady-state macroscopic profiles such as temperature and tracer density do not depend on δ , but δ can have a significant impact on the numerical values of spatial and temporal correlations. In this paper, we have chosen to simplify matters by *fixing* δ , which throughout the paper is set equal to $\frac{1}{10}$.

At any moment in time, the number of tracers at each site can vary from 0 to ∞ . Observe also that the interaction in this simple model is highly nonlinear, even though there are no direct tracer-tracer or tank-tank interactions: tracers at the same site exchange energy via interacting with the tank, and all actions — including energy exchanges and site-to-site jumps — take place at rates proportional to the “speeds” (the square roots of the kinetic energies) of the tracers at that moment in time. This is essential if these stochastic models are to mimic the behaviors of their Hamiltonian counterparts.

1.2 Invariant Measures at Equilibrium

At equilibrium, *i.e.*, when the left and right baths have equal temperatures and injection rates, the invariant measure of the random halves model is known explicitly. To give its density, we need a little bit of notation: the state of a single cell in which there are exactly k tracers is specified by $(S, \{e_1, e_2, \dots, e_k\})$ where $S > 0$ is the stored energy, *i.e.*, the energy of the tank, and $\{e_1, e_2, \dots, e_k\}$ is an unordered set of k positive numbers representing the k tracer energies¹. Let Ω_k denote the set of all possible states of a single cell with exactly k tracers present. The state space for a single cell is then the disjoint union $\Omega = \cup_k \Omega_k$.

¹It is an unordered set because the tracers are indistinguishable.

Proposition 1.1. [9] Let $T_L = T_R = T$, and $\rho_L = \rho_R = \rho$. Then the unique invariant probability measure of the N -chain is the N -fold product

$$\mu_N = \mu^{T,\rho} \times \cdots \times \mu^{T,\rho}$$

where $\mu^{T,\rho}$ is the measure giving the statistics within each cell. The measure $\mu^{T,\rho}$ is defined by:

(i) The number of tracers present is a Poisson random variable with mean $\kappa \equiv 2\rho\sqrt{\pi/T}$, i.e.,

$$\mu^{T,\rho}(\Omega_k) = p_k := \frac{\kappa^k}{k!} e^{-\kappa}, \quad k = 0, 1, 2, \dots \quad (2)$$

(ii) The conditional density of $\mu^{T,\rho}$ on Ω_k is $c_k \sigma_k(\{e_1, \dots, e_k\}, S)$ where

$$\sigma_k(\{e_1, \dots, e_k\}, S) = \frac{1}{\sqrt{e_1 \cdots e_k}} e^{-\beta(e_1 + \dots + e_k + S)}; \quad (3)$$

here $\beta = 1/T$, and $c_k = \beta k! (\beta/\pi)^{k/2}$ is the normalizing constant.

Proposition 1.1 shows that at equilibrium, the stored energies at different sites are entirely uncorrelated. A generalization of this result is given in Proposition 5.1.

1.3 Macroscopic Equations of Nonequilibrium Steady States

We now fix arbitrary boundary conditions T_L, T_R, ρ_L , and ρ_R , and give the equations of temperature and tracer profiles in nonequilibrium steady states.

Assumption 1. We assume that for each N , there is a unique invariant probability measure μ_N to which all initial data converge.

Because the energies are unbounded, a tightness argument is needed to guarantee existence. Uniqueness should be straightforward. In what follows, the word ‘‘mean’’ refers to expectation with respect to μ_N . We identify each site i with the point $x_i = \frac{i}{N+1}$ in the unit interval, and think of $x_0 = 0$ and $x_{N+1} = 1$ as the locations of the baths. For $i = 1, \dots, N$, define

$$\begin{aligned} \rho(x_i) &= \text{mean number of jumps from site } i \text{ to site } i + 1 \text{ per unit time} \\ &= \text{mean number of jumps from site } i \text{ to site } i - 1 \text{ per unit time;} \\ q(x_i) &= \text{mean energy flow from site } i \text{ to site } i + 1 \text{ per unit time} \\ &= \text{mean energy flow from site } i \text{ to site } i - 1 \text{ per unit time.} \end{aligned}$$

That is to say, the mean number of jumps out of site i per unit time is $2\rho(x_i)$; half go to the right and half to the left, and so on. The quantities ρ and q are well-defined in steady state and have very simple behavior:

Lemma 1.1. [9] With ρ and q defined as above, we have, for $x = x_i, i = 1, \dots, N$,

- (i) $\rho(x) = \rho_L + (\rho_R - \rho_L)x;$
- (ii) $q(x) = \rho_L T_L + (\rho_R T_R - \rho_L T_L)x.$

As $N \rightarrow \infty$, these functions converge (trivially) to linear or, more accurately, affine functions on $(0, 1)$. Note that ρ' and q' are the steady-state tracer and energy currents, respectively. These currents by themselves, however, do not determine steady state profiles such as those for temperature and tracer density. The following assumption is used to deduce such information:

Assumption 2. (A version of LTE) For $1 \leq i \leq N$, let $\mu_{N,i}$ denote the marginal of μ_N at the site i . We assume that for every $x \in (0, 1)$, $\mu_{N,[xN]}$ converges as $N \rightarrow \infty$ to $\mu^{T,\rho(x)}$ for some $T = T(x) > 0$. A tightness condition for all the $\mu_{N,[xN]}$ is also assumed.

Let k_i denote the number of tracers present at site i . Recall that S_i is the stored energy.

Theorem 1. [9] Let arbitrary boundary conditions T_L, T_R, ρ_L, ρ_R be given. Under Assumptions 1 and 2,

$$T(x) = \lim_{N \rightarrow \infty} \mathbb{E}_{\mu_N}(S_{[xN]}) \quad \text{and} \quad \kappa(x) = \lim_{N \rightarrow \infty} \mathbb{E}_{\mu_N}(k_{[xN]}) \quad (4)$$

are well-defined and are given by

$$T(x) = \frac{q(x)}{\rho(x)} \quad \text{and} \quad \kappa(x) = 2\sqrt{\pi} \cdot \frac{\rho(x)}{\sqrt{T(x)}}. \quad (5)$$

See [9] for details.

2 Global Fluctuations and Pair Correlations

This paper concerns the spatial energy covariances at steady state of the random halves model described in Sect. 1.1. More precisely, let boundary conditions T_L, T_R, ρ_L and ρ_R be specified, and consider an N -chain. The quantities of interest are

$$\text{Cov}_N(S_i, S_j) = \mathbb{E}_{\mu_N}(S_i S_j) - \mathbb{E}_{\mu_N}(S_i) \mathbb{E}_{\mu_N}(S_j), \quad 1 \leq i, j \leq N, \quad i \neq j.$$

We begin by examining how these quantities scale with N .

2.1 Scaling of Total-Energy Variance

For an N -chain with boundary conditions T_L, T_R, ρ_L and ρ_R , we consider the total energy variance

$$V(N; T_L, T_R, \rho_L, \rho_R) = \text{Var}\left(\sum_{i=1}^N S_i\right). \quad (6)$$

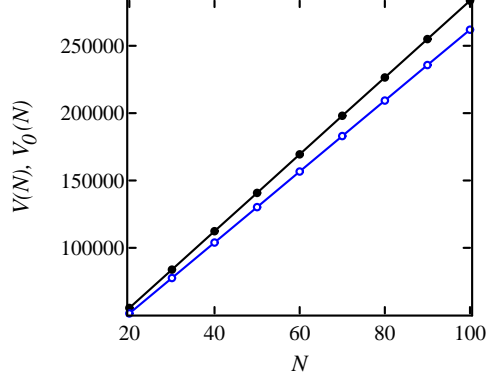


Figure 2: Variance of total energy as function of system size. The upper curve is $V(N)$, the lower curve is $V_0(N)$. The boundary conditions are $T_L = 10$, $T_R = 100$, $\rho_L = 20$, and $\rho_R = 10$.

Keeping the boundary conditions fixed, we treat $V = V(N)$ as a function of N , and observe that $V = V_0 + V_1$ where

$$V_0 = \sum_{i=1}^N \text{Var}(S_i) \quad \text{and} \quad V_1 = \sum_i \sum_{j \neq i} \text{Cov}_N(S_i, S_j). \quad (7)$$

By Theorem 1,

$$\lim_{N \rightarrow \infty} \frac{1}{N} V_0(N) = \int_0^1 T(x)^2 dx. \quad (8)$$

That is, $V_0(N) \sim B_0 N$ for $N \gg 1$ with $B_0 = \int_0^1 T(x)^2 dx$.

When $T_L = T_R$, $V_1 \equiv 0$ (see Sect. 1.2), so that $V(N) = V_0(N) + V_1(N) \sim N$. We expect this to be true when $T_L \neq T_R$ on physical grounds, which leads to the question: is it true that $V_1(N) \sim B_1 N$, and if so, what is the sign of B_1 ? Two sets of numerical simulations are performed to resolve this. In one, we compute $V_1 = V - V_0$ directly as a function of N . In the other, we start from equilibrium, and hope to observe a quadratic response as a temperature gradient is introduced; the sign of the quadratic term is then the sign of B_1 . The reason we expect a quadratic (as opposed to linear) response is symmetry: the temperature gradients $T_R - T_L = \Delta T$ and $T_R - T_L = -\Delta T$ clearly lead to the same energy variances and covariances.

Simulation 1. Fix bath temperatures T_L, T_R and injection rates ρ_L, ρ_R and compute $V(N)$ and $V_0(N)$ for increasing N .

The results, plotted in Fig. 2, show that

$$V(N) \sim BN \quad \text{with} \quad B > B_0 > 0, \quad (9)$$

i.e. $V_1(N) \sim B_1 N$ for some $B_1 > 0$.

Simulation 2. Fix N , $\rho_L = \rho_R$, and a number $m > 0$. Compute V and V_0 for various pairs (T_L, T_R) chosen so that $\frac{T_L + T_R}{2} = m$, and investigate $V_1 = V - V_0$ as a function of $\Delta T = T_R - T_L$.

The results show that V_1 depends quadratically on ΔT with a strictly positive coefficient. Taken together, these two simulations suggest that for $\rho_L = \rho_R$ and fixed mean temperature,

$$V_1(N; T_L, T_R, \rho_L, \rho_R) \propto (T_R - T_L)^2 \cdot N, \quad (10)$$

at least when $|T_R - T_L|$ is not too large compared to the mean temperature in the chain. We will see later that both the linear scaling of V_1 with system size and its quadratic response to temperature gradient are consistent with the scaling of $\text{Cov}_N(S_i, S_j)$.

Note that one advantage of probing spatial correlations via global quantities such as V_1 is that it can be computed more reliably than small, local quantities such as $\text{Cov}_N(S_i, S_j)$.

2.2 Pair Covariances

We begin now to investigate the individual terms in the sum $V_1 = \sum_i \sum_{j \neq i} \text{Cov}_N(S_i, S_j)$.

The two most basic characteristics of $\text{Cov}_N(S_i, S_j)$ are its *sign* and *order of magnitude*. The fact that $V_1(N) \sim N$ suggests that many of the covariances are positive. Indeed, all of our numerical evidence points to $\text{Cov}_N(S_i, S_j) \geq 0$, as does the theoretical reasoning in the sections to follow. There is reason to remain cautious, however: Since $\text{Cov}_N(S_i, S_j) = 0$ when the system is in equilibrium (Proposition 1.1), and can be zero even when there is a tracer flux (Proposition 5.1), one cannot conclude definitively via numerics alone that there are no strictly negative correlations. See the remark at the end of this subsection on why the nonnegativity of covariances in this model may be a delicate question.

We proceed to an analysis of the order of magnitude of $\text{Cov}_N(S_i, S_j)$, assuming in the heuristic discussion below that $\text{Cov}_N(S_i, S_j) \geq 0$ for all i, j .

We propose to decompose V_1 into

$$V_1 = \sum_i V_{1,i} \quad \text{where} \quad V_{1,i} = \sum_{j \neq i} \text{Cov}_N(S_i, S_j)$$

and reason as follows:

- (i) For i away from the two ends of the chain, $V_{1,i} \sim 1$ since these terms sum to $V_1 \sim N$ and it is unlikely that they scale differently with N . (For i close to the boundary, $V_{1,i}$ may be smaller due to the entrance of tracers with *i.i.d.* energies.)
- (ii) For each fixed i , the function $j \mapsto \text{Cov}_N(S_i, S_j)$ should decrease monotonically as $|i - j|$ increases: sites farther apart are expected to be less correlated because they “communicate” via longer and noisier “channels.”

These considerations imply that $\text{Cov}_N(S_i, S_{i+1})$, with i away from 0 and N , are among the larger of the $\sim N^2$ terms in V_1 . Since $\text{Cov}_N(S_i, S_{i+1})$ is one of N terms in $V_{1,i}$, (i) above implies

$$\text{Cov}_N(S_i, S_{i+1}) \gtrsim \frac{1}{N}.$$

We point out that the order of magnitude of $\text{Cov}_N(S_i, S_{i+1})$ contains a fair amount of information about the shape of the function $j \mapsto \text{Cov}_N(S_i, S_j)$: if $\text{Cov}_N(S_i, S_{i+1}) \sim \frac{1}{N}$, then

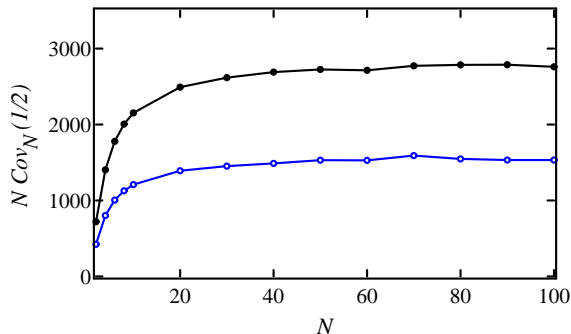


Figure 3: Scaling of Cov_N with N . This plot shows $N \cdot \text{Cov}_N(S_{[N/2]}, S_{[N/2]+1})$ as a function of N . Boundary conditions are $T_L = 10$, $T_R = 190$, and $\rho_L = \rho_R = 20$ for the upper curve and $\rho_L = \rho_R = 40$ for the lower one.

$\text{Cov}_N(S_i, S_j) \sim \frac{1}{N}$ for a definite fraction of j (because these terms have to add up to ~ 1). This points to an extremely slow decay of $\text{Cov}_N(S_i, S_j)$ with increasing distance between sites i and j . If, on the other hand, $\text{Cov}_N(S_i, S_{i+1}) \gg \frac{1}{N}$, then the function $j \mapsto \text{Cov}_N(S_i, S_j)$, $j \neq i$, would have a very sharp peak at $j = i \pm 1$. The question is: which scenario is the case here?

To resolve this issue, we perform the following numerical simulation:

Simulation 3. For fixed boundary conditions, compute $\text{Cov}_N(S_{[N/2]}, S_{[N/2]+1})$ for a range of N .

Two sets of results are plotted in Fig. 3. They (and other data sets not shown here) show that

$$\text{Cov}_N(S_{[N/2]}, S_{[N/2]+1}) \sim \frac{1}{N}. \quad (11)$$

As explained above, one may infer from this that all pair covariances $\text{Cov}_N(S_i, S_j) = O(1/N)$, a fact confirmed by many subsequent simulations (see *e.g.* Fig. 12).

Remarks on sign of $\text{Cov}_N(S_i, S_j)$. As far as we know, existing analytic techniques for proving or disproving positivity of correlations do not apply to the random halves model. This, in part, is due to the fact that in our model, mechanisms conducive to both positive and negative correlations are at work, and the actual covariance reflects a balance between these two tendencies. For instance, a large, upward surge in the energies of incoming tracers has the effect of raising some of the stored energies above their expected values. It is believed that such excursions lead to long-wavelength fluctuations with slow relaxation times, resulting in positive correlations [10]. However, upon interacting with one of the tanks, a tracer that acquires a higher-than-normal fraction of the energy is likely to move more quickly to a neighboring site and to interact with the tank there, possibly transferring its energy to the tank in its new location. Such a phenomenon creates negative correlations between neighboring sites. In equilibrium, these two tendencies balance perfectly, giving zero covariance (see Proposition 1.1). Further numerical evidence in support of nonnegative covariances is given in Sect. 5.1.

3 Covariance Structures “at $N = \infty$ ”

The purpose of this short section is to make explicit the objects to be studied in the rest of this paper and the assumptions under which we plan to operate.

The discussion in the Sect. 2.2 points to the following functions: Given boundary conditions T_L, T_R, ρ_L and ρ_R , and $x, y \in (0, 1)$, $x \neq y$, define $\mathcal{C}(x)$ and $\mathcal{C}_2(x, y)$ by

$$\begin{aligned}\mathcal{C}(x) &= \mathcal{C}(x; T_L, T_R, \rho_L, \rho_R) = \lim_{N \rightarrow \infty} N \cdot \text{COV}_N(S_{[xN]}, S_{[xN]+1}), \\ \mathcal{C}_2(x, y) &= \mathcal{C}_2(x, y; T_L, T_R, \rho_L, \rho_R) = \lim_{N \rightarrow \infty} N \cdot \text{COV}_N(S_{[xN]}, S_{[yN]}),\end{aligned}$$

if these limits exist.

Supposing these functions are well defined, it is natural to ask (i) how $\mathcal{C}(x)$ depends on local thermodynamic quantities such as $T(x)$, $\kappa(x)$ and their gradients, and (ii) if these local quantities completely determine $\mathcal{C}(x)$. We present below an answer to the second question; it is one of a number of possible answers. Question (i) is addressed in the next two sections.

Given $x \in (0, 1)$ and $(T_L, T_R, \rho_L, \rho_R)$, Theorem 1 gives a quadruple $(T_*, \rho_*, T'_*, \rho'_*)$ where $T_* = T(x)$, $\rho_* = \rho(x)$, $T'_* = T'(x)$ and $\rho'_* = \rho'$. Conversely, given $x \in (0, 1)$ and a quadruple $(T_*, \rho_*, T'_*, \rho'_*)$, it is easy to check that one can solve the equations in Theorem 1 backwards and find the corresponding boundary conditions. This one-to-one correspondence between boundary and local conditions defines a function \mathcal{F} with

$$\mathcal{F}(x; T_*, \rho_*, T'_*, \rho'_*) = \mathcal{C}(x; T_L, T_R, \rho_L, \rho_R). \quad (12)$$

Since we work only with finite chains, it is necessary to have a version of \mathcal{F} before the infinite-volume limit. Given $(T_L, T_R, \rho_L, \rho_R)$, x and N , we let $i = [xN]$, and let $T_i, \rho_i, \Delta T_i$ and $\Delta \rho_i$ be as follows: T_i is the mean temperature at site i , ρ_i is the “injection rate” (see Sect. 1.3 for precise definition), $\Delta T_i = T_{i+1} - T_i$ and $\Delta \rho_i = \rho_{i+1} - \rho_i$. Let

$$\mathcal{F}_N \left(x; T_i, \rho_i, \frac{\Delta T_i}{\Delta_N}, \frac{\Delta \rho_i}{\Delta_N} \right) = N \cdot \text{COV}_N(S_i, S_{i+1})$$

where $\Delta_N = \frac{1}{N+1}$. The next lemma shows that the function \mathcal{F}_N is well defined:

Lemma 3.1. *Given $N, i, T_i, \rho_i, \Delta T_i$ and $\Delta \rho_i$, there is a unique set of boundary conditions $(T_L, T_R, \rho_L, \rho_R)$ for the N -chain that leads to these values at site i provided N is sufficiently large (or ΔT_i and $\Delta \rho_i$ are sufficiently small).*

Proof. First, ρ_i and $\Delta \rho_i$ determine ρ_L and ρ_R by linearity of ρ (see Lemma 1.1, §1.3), provided $\Delta \rho_i$ is small enough that both of these numbers are nonnegative. For definiteness, assume $\Delta T_i > 0$. We will find suitable T_L and T_R by varying both until correct values are attained at site i : Fix the left bath temperature temporarily at $\hat{T}_L \in (0, T_i)$, and vary the right bath temperature from T_i to ∞ . Since the temperature at site i increases strictly monotonically with the right bath temperature, there exists a unique $\hat{T}_R = \hat{T}_R(\hat{T}_L) > T_i$ giving the correct value of T_i at site i . Now look at the chain with bath temperatures \hat{T}_L and \hat{T}_R . As \hat{T}_L increases to T_i , ΔT_i decreases to 0, so for ΔT_i sufficiently small, there is a unique T_L for which $T_{i+1} - T_i$ is equal to ΔT_i . \square

With \mathcal{F} and \mathcal{F}_N as above, and for fixed boundary conditions, the limit in the definition of $\mathcal{C}(x)$ is equivalent to

$$\lim_{N \rightarrow \infty} \mathcal{F}_N \left(x; T_i, \rho_i, \frac{\Delta T_i}{\Delta_N}, \frac{\Delta \rho_i}{\Delta_N} \right) = \mathcal{F}(x; T_*, \rho_*, T'_*, \rho'_*). \quad (13)$$

Such a limit involves difficult issues beyond the scope of this paper. For example, while the convergence of T_i to T_* as $N \rightarrow \infty$ follows from LTE (Assumption 2), the convergence of $\frac{\Delta T_i}{\Delta_N}$ to T'_* cannot be deduced from previous assumptions.

In addition to Assumptions 1 and 2 in Sect. 1.3, we now introduce two other sets of assumptions on which the rest of our analysis relies.

Assumption 3. *The functions \mathcal{C} and \mathcal{C}_2 are well defined and finite-valued.*

Assumption 4. (i) *In the context of (13), $\frac{\Delta T_i}{\Delta_N} \rightarrow T'_*$ as $N \rightarrow \infty$.*

(ii) *The function \mathcal{F} defined by (12) is differentiable.*

Assumption 3 asserts the presence of a well-defined structure at “ $N = \infty$ ” that governs the covariance relationships of the invariant measures μ_N for large N . Such a structure goes beyond the idea of LTE to treat information of the next order, namely how μ_N deviates from local equilibrium at microscopic length scales, and how it deviates from products of Gibbs measures (at varying local temperatures) globally. Assumption 4 identifies some technical issues which we take for granted.

4 Covariances at Microscopic Distances: $\rho_L = \rho_R$

This section and the next concern nearest-neighbor covariances in long chains, *i.e.* $\text{COV}_N(S_i, S_{i+1})$ for large N . We treat in this section the simpler case where there is no tracer flux in the system; the equality $\rho_L = \rho_R = \rho$ is assumed throughout. Our aim is to discover how the functions \mathcal{C} , equivalently \mathcal{F} , depend on the various quantities.

4.1 The two middle sites

In this subsection, we fix $x = \frac{1}{2}$, and study the function $(T, \rho, T') \mapsto \mathcal{F}(\frac{1}{2}; T, \rho, T', 0)$ where \mathcal{F} is as defined in Sect. 3. Here T, ρ and T' are quantities associated with the midpoint of the chain; in particular, T' is the temperature gradient at $x = \frac{1}{2}$. We begin by examining the dependence of \mathcal{F} on T' . Fix T and ρ , and consider

$$F(T') = F^{T, \rho}(T') = \mathcal{F}\left(\frac{1}{2}; T, \rho, T', 0\right). \quad (14)$$

That is to say, $F(T') \approx N \cdot \text{COV}_N(S_{[N/2]}, S_{[N/2]+1})$ for large N with boundary conditions $T_L = T - \frac{1}{2}T'$, $T_R = T + \frac{1}{2}T'$ and $\rho_L = \rho_R = \rho$. Clearly, $F(0) = 0$, and F is an even function due to the left-right symmetry. This leads one to expect a quadratic response when the system is taken out of equilibrium. The following simulation confirms that the coefficient of the quadratic term is indeed nonzero.

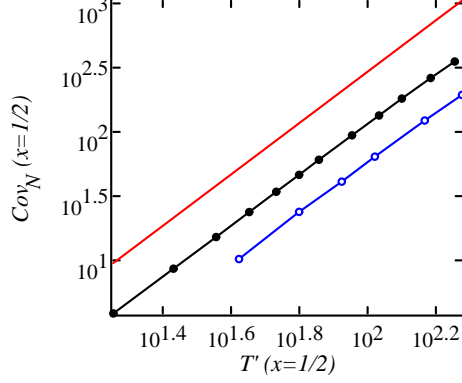


Figure 4: Scaling of middle-pair covariance with temperature gradient. The plot shows $\text{Cov}_N(S_{[N/2]}, S_{[N/2]+1})$ as a function of T' on a logarithmic scale. Boundary conditions are chosen to fix $T = 60$ and $\kappa = 2.5\sqrt{\pi}$ at $x = \frac{1}{2}$. Solid discs: $N = 8$; open circles: $N = 20$. A solid line of slope 2 is shown for reference. See Appendix A for a discussion of simulation parameters.

Simulation 4. For various pairs of T and ρ , compute $\text{Cov}_N(S_{[N/2]}, S_{[N/2]+1})$ for a sample of T' .

A set of results are plotted in Fig. 4. The data show that (i) $\frac{\partial^2 F}{\partial T'^2}(0) \neq 0$, and in fact, (ii) $F(T')$ is fairly well approximated by a quadratic function over the entire range $(-2T, 2T)$ of T' . (The minimum temperature tends to 0 as $|T'| \rightarrow 2T$.) Note that if $F(T')$ is smooth, then the only other possibility is $F(T') \sim T'^{2k}$ for some $k \in \{2, 3, \dots\}$, which is clearly not the case here. Other data sets (not shown) with different values of (T, ρ) confirm these conclusions.

We investigate next the dependence of $a(T, \rho) := \frac{1}{2} \frac{d^2 F}{dT'^2}(0)$ on T and ρ . First, we establish a simple result (which is expected from dimensional analysis):

Lemma 4.1. Fix T and ρ , and view $\lambda > 0$ as a parameter. Define $F^{T, \rho}$ and $F^{\lambda^2 T, \lambda \rho}$ as in (14). Then

$$F^{\lambda^2 T, \lambda \rho}(\lambda^2 T') = \lambda^4 F^{T, \rho}(T'). \quad (15)$$

Proof. Given T, ρ and T' , let T_L, T_R and $\rho_L = \rho_R$ be the boundary conditions that give rise to these values at the two middle sites, and consider a second system with boundary conditions $\lambda^2 T_L, \lambda^2 T_R$ and $\lambda \rho_L = \lambda \rho_R$ and initial tank energies λ^2 times those of the first system. Via a standard coupling argument, the sample paths for these two systems are easily matched. Corresponding sample paths give rise to time evolutions with identical tracer counts in both systems – but with the second system at energies λ^2 times that of the first and running at speeds λ times that of the first. This leads to (15). \square

Let $F^{\lambda^2 T, \lambda \rho}(T') \approx a_\lambda T'^2$. It follows from Lemma 4.1 that

$$a_\lambda \cdot (\lambda^2 T')^2 \approx F^{\lambda^2 T, \lambda \rho}(\lambda^2 T') \approx \lambda^4 F^{T, \rho}(T') \approx \lambda^4 a_1 T'^2. \quad (16)$$

Thus a_λ is independent of λ , and $F^{T, \rho}(T')$ can be written as $F^\kappa(T')$ where $\kappa = 2\rho\sqrt{\pi/T}$ is the mean tracer count with respect to $\mu^{T, \rho}$ (see Sect. 1.2). The preceding argument tells us that for any T, ρ, κ related as above, the function $A(\kappa) := a(T, \rho)$ is well-defined, and

$$\text{Cov}_N(S_{N/2}, S_{N/2+1}) \approx \frac{1}{N} A(\kappa) T'^2. \quad (17)$$

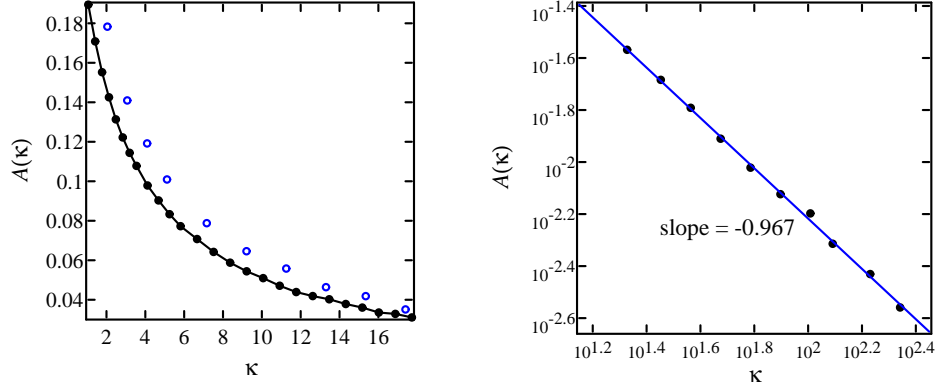


Figure 5: The A -curve computed using 8-chains. The boundary conditions are $T_L = 20$, $T_R = 30$, and $\rho_L = \rho_R = 2.5\kappa/\sqrt{\pi}$, and $A(\kappa)$ is estimated using Eq. (17) with $N = 8$. **Left:** Linear plot. Also shown are some points computed using 16-chains (open circles; $T_L = 50$, $T_R = 100$, and $\rho_L = \rho_R = 5\kappa/\sqrt{2\pi}$). **Right:** Log-log plot shows that $A(\kappa) \sim 1/\kappa$ for $\kappa \gg 1$.

A natural question is how $A(\kappa)$ depends on κ . Other things being equal, one would think intuitively that local thermal fluctuations are smaller when more tracers are present, because stored energy is affected less by the entrance of a tracer with very large or very small energy. To confirm this, and to collect data for later use, we compute the function A . Practical reasons dictate that very short chains be used due to the large number of data points (each one of which requiring a separate run) and the time it takes for covariances to converge in long chains; see Appendix A for a discussion of relevant numerical issues. However, some understanding of the errors introduced by the use of very short chains is necessary if these data are to be useful in later predictions.

Simulation 5. Compute $A(\kappa)$ systematically for a range of κ using chains of 8 cells. Compute also some values of $A(\kappa)$ using 16-chains for comparison.

The 8-chain results are shown in Fig. 5. Note that the function decreases monotonically as expected, and $A(\kappa) \sim 1/\kappa$ as $\kappa \rightarrow \infty$.

Let $A_8(\kappa)$ and $A_{16}(\kappa)$ denote the values of $A(\kappa)$ computed using 8 cells and 16 cells respectively. We computed $A_{16}(\kappa)$ for some values of κ , and find these values to be somewhat larger than the corresponding values for A_8 . This is consistent with Fig. 3, and the true A -values (defined at “ $N = \infty$ ”) are likely to be larger still. We find, however, that the *ratios* of the two sets of values remain fairly constant as κ varies. For example,

$$1.14 < A_{16}(\kappa)/A_8(\kappa) < 1.20 \quad \text{for } \kappa \in [2\sqrt{\pi}, 10\sqrt{\pi}].$$

We will use the 8-chain A -curve data in our study of long-chain covariances. All of our long-chain simulations involve κ in subintervals of the range shown above, and we will only assume that $A(\kappa) \approx \text{const} \cdot A_8(\kappa)$.

4.2 Quadratic responses to local temperature gradients

We demonstrated in Sect. 4.1 that at $x = \frac{1}{2}$, the response to the local temperature gradient T' is quadratic. We now examine the situation at $x \neq \frac{1}{2}$. Recall that our argument for showing that

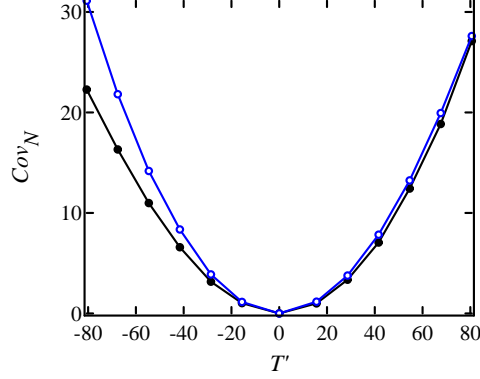


Figure 6: Quadratic response to T' at $x \neq \frac{1}{2}$. We fix $x \neq 1/2$ and set $T(x) = 60$, $\kappa(x) = 5\sqrt{\pi}$. We then compute $\text{Cov}_N(S_{[xN]}, S_{[xN]+1})$ as a function of $T'(x)$. Solid discs: $x \approx 0.27$; open circles: $x \approx 0.65$. Here, we use $N = 12$. We do not take T' much smaller than the values shown for reasons discussed in Appendix A.

the leading term has order ≥ 2 at $x = \frac{1}{2}$ uses the left-right symmetry of the chain, a property not present at $x \neq \frac{1}{2}$. Reasoning physically, however, it is hard to imagine that the response to local temperature gradient is sometimes quadratic, sometimes linear, or that the coefficient of the linear term would vanish at exactly $x = \frac{1}{2}$ independent of boundary conditions. The following simulation confirms this thinking.

Simulation 6. For fixed $x \in (0, 1)$, $T = T(x)$ and ρ , compute $\text{Cov}_N(S_{[xN]}, S_{[xN]+1})$ for various values of $T' = T'(x)$. Repeat for various $x \neq \frac{1}{2}$.

Fig. 6 shows the results for some values of x . The function $T' \mapsto \mathcal{F}(x; T, \rho, T', 0)$ for fixed x , T , and ρ is clearly quadratic to leading order and contains a nonzero third-order term (which is not present when $x = \frac{1}{2}$). Other sets of data, computed using different values of T and ρ , lead to the same conclusion.

Notice that a quadratic response to T' is consistent with the observation in Sect. 2.1 that $\sum_{i \neq j} \text{Cov}_N(S_i, S_j) \propto (T_R - T_L)^2 \cdot N$.

4.3 Boundary effects

In Sects. 4.1 and 4.2, we showed that (i) for each fixed x , T , and ρ , $\mathcal{F}(x; T, \rho, T', 0) \sim T'^2$ (at least for $|T'|$ not too large); and (ii) at $x = \frac{1}{2}$, the coefficient in front of T'^2 is a function of $\kappa(\frac{1}{2})$, that is to say, $\mathcal{F}(\frac{1}{2}; T, \rho, T', 0) \approx A(\kappa(\frac{1}{2})) \cdot T'(\frac{1}{2})^2$, the function $A(\kappa)$ being *defined* by this relation at $x = \frac{1}{2}$. With $A(\cdot)$ so defined, we now ask if the same relation holds at every $x \in (0, 1)$, *i.e.*, if it is true that $\mathcal{F}(x; T, \rho, T', 0) \approx A(\kappa(x)) \cdot T'(x)^2$.

Consider, for the moment, a different situation in which the system is infinite in length, *i.e.*, $x \in (-\infty, \infty)$, and a temperature gradient is maintained by, say, a constant external field. One would expect such a system to be translation-invariant, which implies that $\text{Cov}_N(S_{[xN]}, S_{[xN]+1}) = \text{Cov}_N(S_{[yN]}, S_{[yN]+1})$ if the quantities $A(\kappa)T'^2$ at x and y are identical, *i.e.*, we would expect the answer to the question above to be affirmative.

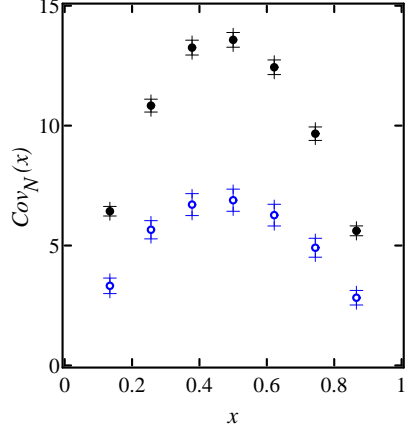


Figure 7: Covariances with identical local conditions at various x . For each x , we choose boundary conditions so that $T(x) = 60$, $T'(x) = 60$, $\rho \approx 7.75$ (closed discs) and 19.4 (open discs). With these local conditions, we compute $\text{Cov}_N(S_{[xN]}, S_{[xN]+1})$ for various x symmetrically placed about $x = \frac{1}{2}$. Note that each point requires a separate simulation. Here, $N = 40$. We include 1-standard deviation error bars; see Appendix A for factors affecting the numerical accuracy of computations.

Our system has no translation invariance to speak of and, at least for finite N , the randomizing effects of the baths are apparent: nearest-neighbor covariances are significantly smaller near the boundaries because the baths inject tracers with *i.i.d.* sequences of energies into the system. The answer to the question posed above depends on how fast these randomizing effects dissipate. Do they decrease by a certain amount per lattice site, or do they decrease with macroscopic distance? The aim of the following simulation is to shed light on these questions.

Simulation 7. Fix a triplet (T_*, ρ_*, T'_*) and compute $\text{Cov}_N(S_{[xN]}, S_{[xN]+1})$ for various x , using (T_*, ρ_*, T'_*) as the local conditions at x . That is, for each x , we first compute boundary conditions which give $T(x) = T_*$, $T'(x) = T'_*$, and $\rho(x) = \rho_*$, and then use these boundary conditions to compute the pair covariance at x . Repeat for various choices of (T_*, ρ_*, T'_*) .

The results, shown in Fig. 7, show clearly that the randomizing effects of baths dissipate in a manner more like a diffusion process than by a definite amount per lattice site. Note also the asymmetry of the data points: identical local conditions at x and $1 - x$ do not produce equal covariance relations. This suggests that from the conduction point of view, effective distance from the boundary may not equal physical distance.

To capture the phenomenon observed, we introduce, for given boundary conditions T_L, T_R and $\rho_L = \rho_R = \rho$, a function $\varphi^{bc}(x)$ defined by the expression

$$\mathcal{C}(x) = \varphi^{bc}(x) \cdot A(\kappa(x))T'(x)^2, \quad x \in (0, 1). \quad (18)$$

We add the superscript “bc” to stress the fact that this function depends on boundary conditions. By definition, $\varphi^{bc}(\frac{1}{2}) \rightarrow 1$ as $T'(\frac{1}{2}) \rightarrow 0$. Since we do not know of any other forces acting on the system, we think of $\varphi^{bc}(x)$ as a measure of the randomizing effects of the baths at location x , and continue our investigation based on this thinking.

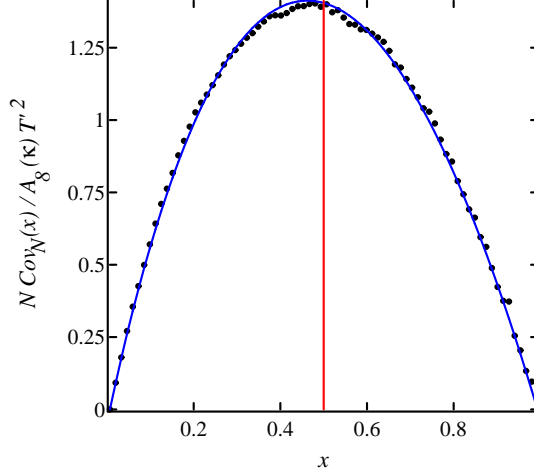


Figure 8: Comparison of φ^{bc} and $\hat{\varphi}^{bc}$. The boundary conditions here are $T_L = 5$, $T_R = 45$, $\rho_L = \rho_R = 8$, and $N = 60$. We estimate $\varphi^{bc}(x)$ by $N \cdot \text{Cov}_N(S_{[xN]}, S_{[xN]+1}) / A_8(\kappa) T^2$ where A_8 denotes the 8-chain A -curve computed in Simulation 5, and plot the resulting curve against $y = c\tau(x)$ where c is chosen to minimize the (unweighted) least-squares distance between the two curves. A vertical line is placed at $x = \frac{1}{2}$ for reference. **Clarifications:** (i) As noted at the end of Sect. 4.1, there is a number $c_1 > 1$ such that the $A \approx c_1 \cdot A_8$. Thus the data points here represent empirical values of $c_1 \varphi^{bc}$. The constant c_1 is absorbed into the choice of c , so that the solid curve can be thought of as $c_1 \hat{\varphi}^{bc}$. (ii) A least-square minimization is used instead of setting the functions equal at $x = \frac{1}{2}$ as prescribed in the text because the data near $x = \frac{1}{2}$ are visibly unconverged.

We now seek to identify the function $\varphi^{bc}(x)$. To capture the idea of “effective distance to boundary,” we introduce the following *time-to-boundary* functions:² in an N -chain, let $\tau_i^{(N)}$ denote the expected time for a tracer at site i to reach one of the baths. We then have the relation

$$\tau_i^{(N)} = \frac{1}{\sqrt{T_i}} + \frac{1}{2} \left(\tau_{i-1}^{(N)} + \tau_{i+1}^{(N)} \right) \quad (19)$$

where T_i is the temperature profile and $\frac{1}{\sqrt{T_i}}$ the expected time a tracer spends at site i . Identifying the i th site with $x_i = \frac{i}{N+1} \in (0, 1)$ and letting $\tau = \frac{1}{N^2} \tau^{(N)}$, we obtain, as $N \rightarrow \infty$, the differential equation

$$\tau''(x) = -\frac{2}{\sqrt{T(x)}}, \quad \tau(0) = \tau(1) = 0. \quad (20)$$

We define

$$\hat{\varphi}^{bc}(x) := \text{const } \tau(x) \quad (21)$$

where τ is the solution of (20) and the constant is chosen so that $\hat{\varphi}^{bc}(\frac{1}{2}) = \varphi^{bc}(\frac{1}{2})$, and conjecture that φ^{bc} is approximately equal to $\hat{\varphi}^{bc}$. Note that $\hat{\varphi}^{bc}$ also depends on boundary conditions. We now test this conjecture numerically:

²Implicit here is the idea of a dual particle system similar to that for *e.g.* the KMP model. We do not know if such a dual system can be constructed for the random halves model.

Simulation 8. Fix boundary conditions and N . For $x \in (0, 1)$, estimate $\varphi^{bc}(x)$ by computing $\text{Cov}_N(S_{[xN]}, S_{[xN]+1})$ and dividing the result by $\frac{1}{N}A(\kappa)T'^2$. Compare the resulting function to $\hat{\varphi}^{bc}(x)$.

The results are displayed in Fig. 8. They show that to the degree that we are able to estimate these functions accurately, the two graphs are in near-perfect agreement. These graphs are not far from a perfect parabola, but the definitive presence of asymmetry – in both Fig. 7 and Fig. 8 – provides convincing evidence that at comparable distances, it takes longer to reach the bath at the lower-temperature end of the chain.

Remark. When the system is in equilibrium, *i.e.*, when $T_L = T_R = T$, the solution of (20) is easily computed to be $\tau(x) = \frac{1}{\sqrt{T}}x(1-x)$. Recall that the expression $x(1-x)$ also appears in the formulas for spatial covariances in the simple exclusion [7, 20] and KMP models [3]. An important difference between these models and ours is that there, the clocks signaling state changes ring at rate 1, whereas in ours, they ring at energy-dependent rates. This property is responsible for, among other things, the slight asymmetry in τ .

From the limited data available, we clearly cannot conclude the validity of our conjecture, but details aside, the general ideas seem to point in the right direction.

5 Covariances at Microscopic Distances: $\rho_L \neq \rho_R$

We return to the general case where both energy and tracer fluxes may be present. The situation here is more complex, and we are less able to separate the contributions of the various factors. We will focus on the dominant effects, and make some observations along the way.

5.1 Responses to local gradients

As before, we consider first $x = \frac{1}{2}$. For fixed T and ρ , we consider the function

$$F(T', \rho') = F^{T, \rho}(T', \rho') = \mathcal{F}\left(\frac{1}{2}; T, \rho, T', \rho'\right)$$

and begin with a few observations on which terms may be absent in its Taylor series.

Proposition 5.1. $F(0, \rho') \equiv 0$ for all ρ' .

Proof. Using the notation in Sect. 1, we claim that when $T' = 0$, the invariant measure μ_N of the chain is the product

$$\mu^{T, \rho_1} \times \mu^{T, \rho_2} \times \dots \times \mu^{T, \rho_N}$$

where $\rho_L = \rho - \frac{1}{2}\rho'$ and $\rho_i = \rho_L + \frac{i}{N+1}\rho'$ for $i = 1, \dots, N$, so that stored energies at distinct sites are uncorrelated. This is proved by direct verification (along the lines of the proof of Proposition 3.7 in [9]). See Appendix B for details. \square

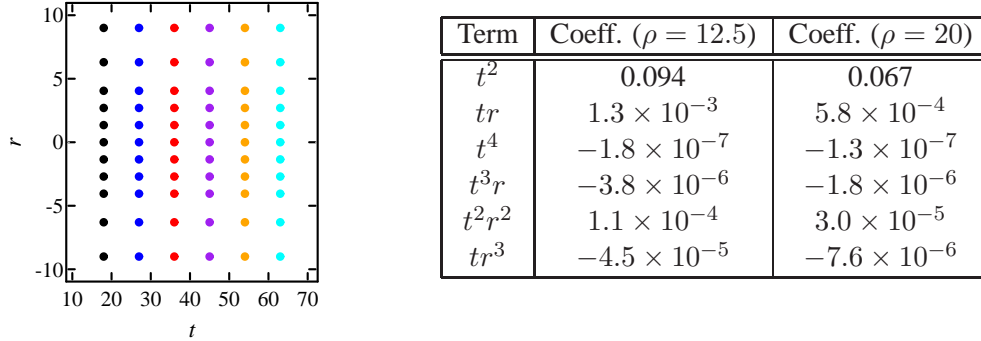


Figure 9: Local polynomial expansion of F . We set $T = 100$, $\rho \in \{12.5, 20\}$, $T' = t$, and $\rho' = r$ at $x = \frac{1}{2}$, then compute $F(t, r) \approx N \cdot \text{Cov}_N(\frac{1}{2})$ for $N = 8$ using the (t, r) values from the grid (**left panel**). We then find the best polynomial (in the sense of least-squares) of the form $at^2 + btr + ct^4 + dt^3r + et^2r^2 + ftr^3$ which fits the data (**right panel**). For both values of ρ , the absolute standard error for the coefficient of the tr term is $\sim 2 \times 10^{-3}$.

Interchanging T_L with T_R and ρ_L with ρ_R , we see that $F(T', \rho') = F(-T', -\rho')$, so that there are no odd order terms in the polynomial approximation of $F(T', \rho')$. Proposition 5.1 says there are no terms that are purely powers of ρ' , and we have shown in Sect. 4.1 that among the terms that are pure powers of T' , the leading one is T'^2 .

Perturbing from equilibrium, we have shown that $\frac{\partial F}{\partial T'}(0, 0) = \frac{\partial F}{\partial \rho'}(0, 0) = 0$. Consider the Hessian $D^2F(0, 0)$. Since $\frac{\partial^2 F}{\partial \rho'^2} = 0$ (Proposition 5.1), it follows that for $|T'|, |\rho'| \ll 1$,

$$F(T', \rho') \approx aT'^2 + bT'\rho', \quad \text{for some } a = a(T, \rho) \text{ and } b = b(T, \rho). \quad (22)$$

Recall our brief discussion of the sign of $\text{Cov}_N(\cdot, \cdot)$ in Sect. 2.2. Our next lemma says that the degeneracy of the Hessian $D^2F(0, 0)$ is equivalent to all covariances at $x = \frac{1}{2}$ having the same sign, namely the sign of $a(T, \rho)$.

Lemma 5.1. $F \geq 0$ in a neighborhood of $(0, 0)$ if and only if $a \geq 0$ and $b = 0$.

Proof. As a quadratic form, the Hessian $D^2F(0, 0)$ has maxima and minima in perpendicular directions. We know already that it is degenerate along the ρ' -axis. Thus either the minimum is negative, that is $F(T', \rho') < 0$ for some (T', ρ') , or the Hessian is positive semi-definite, i.e. $a \geq 0$ and $b = 0$. \square

To determine the leading-order terms of the Taylor expansion of F near $(0, 0)$, in particular to see if $b \equiv 0$ (equivalently $F \geq 0$), we perform the following simulation:

Simulation 9. Fix T and ρ , and set $T' = t$, $\rho' = r$. Compute $F(t, r)$ for a grid of (t, r) values and use the resulting data to find the best fitting 4th degree polynomial of the form

$$P(t, r) = at^2 + btr + ct^4 + dt^3r + et^2r^2 + ftr^3. \quad (23)$$

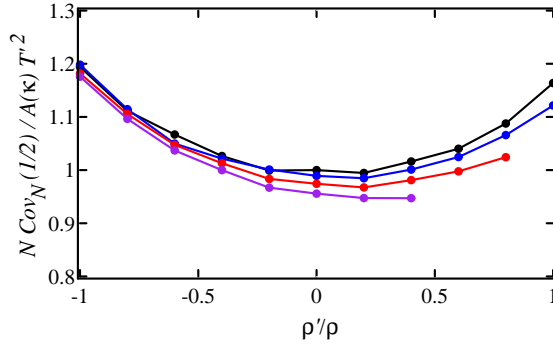


Figure 10: Responses to local gradients for various T' and ρ' at $x = \frac{1}{2}$. We fix T , ρ , and T' at $x = \frac{1}{2}$, then plot $N \cdot \text{Cov}_N(\frac{1}{2})/A(\kappa)T'^2$ as a function of ρ'/ρ . Each curve corresponds to one value of T' . The parameters are $N = 12$, $T(\frac{1}{2}) = 50$, $\rho(\frac{1}{2}) \approx 9.68$, and $T'(\frac{1}{2}) = 90, 70, 50$, and 30 (top to bottom). Some of the curves are discontinued because when $T'(\frac{1}{2})$ and $\rho'(\frac{1}{2})$ are large, $T(x)$, which decreases monotonically with x , may reach 0 before x does. This is easily seen from Theorem 1.

Two sets of results is shown in Fig. 9. We find that in these simulations (and in others not shown here), the leading-order term in the Taylor polynomial of $F(T', \rho')$ is aT'^2 with $a > 0$. In all cases, $|b| \ll 1$, which is consistent with all observed covariances being ≥ 0 . As expected, we cannot conclude definitively that $b \equiv 0$.

From here on we take as a working assumption that the quadratic form associated with $D^2F(0, 0)$ above is degenerate, *i.e.*, at $x = \frac{1}{2}$, the only second order term is $A(\kappa)T'^2$ as in the $\rho_L = \rho_R$ case. For similar reasons as before, namely that the qualitative picture elsewhere in the chain should not differ from that at $x = \frac{1}{2}$, we assume further the absence of $T'\rho'$ -terms in the Taylor expansion of F at all $x \in (0, 1)$. This completes our discussion of how covariance depends on local quantities when the system is not far from equilibrium.

5.2 Far-from-equilibrium corrections

We have shown that at $x = \frac{1}{2}$, $F^{T,\rho}(T', \rho') \approx A(\kappa)T'^2$ is a good approximation of the response to the local temperature and injection gradients – *provided* $|T'|$ and $|\rho'|$ are sufficiently small. In the $\rho' = 0$ case, we noted in Sect. 4.1 that the function $T' \mapsto F^{T,\rho}(T')$ is close but not equal to a perfect quadratic for large T' . We now investigate the effect of larger $|\rho'|$ on $F^{T,\rho}(T', \rho')$.

Simulation 10. For fixed values of (T, ρ) , compute $F^{T,\rho}(T', \rho')$ at $x = \frac{1}{2}$ as a function of T' and ρ' , and study the deviations from the function $A(\kappa)T'^2$.

A set of results is shown in Fig. 10. The results for other choices of (T, ρ) (not shown) are similar.

Observe that (i) the dominant factor is $A(\kappa)T'^2$, but a moderate correction (roughly 20% for $|\rho'/\rho| \leq 1$) to the leading coefficient is sometimes needed; and (ii) a larger $|\rho'|$ tends to increase covariances. Along the lines of the conjectural thinking that positive covariances are caused by waves of abnormally high (or low) energy tracers with long wavelengths, the presence of a tracer flux appears to amplify the propagation of these waves.

5.3 Nearest-neighbor covariances in long chains

We have seen that the presence of a tracer flux complicates the behavior of covariances at $x = \frac{1}{2}$ when the system is far from equilibrium. We do not know how it affects the propagation of boundary effects, or how to separate these contributions (or if they can be separated at all). We will demonstrate in this subsection, however, that the *main ingredients* in $\text{Cov}_N(S_i, S_{i+1})$ are those already identified in Sect. 4.

More precisely, let φ^{bc} and $\hat{\varphi}^{bc}$ be as defined in Sect. 4.3. That is to say, φ^{bc} is as defined in (18), τ the solution of (20), and $\hat{\varphi}^{bc}(x) = c\tau(x)$ where c is chosen to ensure $c\tau(\frac{1}{2}) = \varphi^{bc}(\frac{1}{2})$. We test the validity of

$$\text{Cov}_N(S_{[xN]}, S_{[xN]+1}) \approx \frac{1}{N} \cdot \hat{\varphi}^{bc}(x) \cdot A(\kappa(x)) \cdot T'(x)^2 \quad (24)$$

as an approximate relation.

Simulation 11. *For fixed boundary conditions with $\rho_L \neq \rho_R$, and N taken as large as possible, compare empirically computed values of $\text{Cov}_N(S_i, S_{i+1})$ to their predicted values given by (24).*

The results for two sets of boundary conditions are plotted in Fig. 11. Notice that only the shapes of $\mathcal{C}(x)$ are being predicted because of unknown normalization factors.

Fig. 11 confirms many features of our predictions. First, the shapes of $\mathcal{C}(x)$ confirm that the randomizing effects of the heat baths are diffusive in nature; these effects result in an effective-distance factor whose graph takes the form of a distorted parabola. Second, the locations of the peaks of $\mathcal{C}(x)$ show the influence of T' ; see the left column of Fig. 11.³ Finally, comparison of the data for different N in each set provide another confirmation of the $O(1/N)$ scaling.

Fig. 11 also shows the need for corrective factors on the order of 10 – 15% away from the boundaries. While we do not know the precise nature of these corrections, we point out that in the presence of a tracer flux, the functions φ^{bc} (as computed from empirical data) are a little more asymmetric than in the case $\rho_L = \rho_R$ (shown in Fig. 8).

6 Long-range Covariances

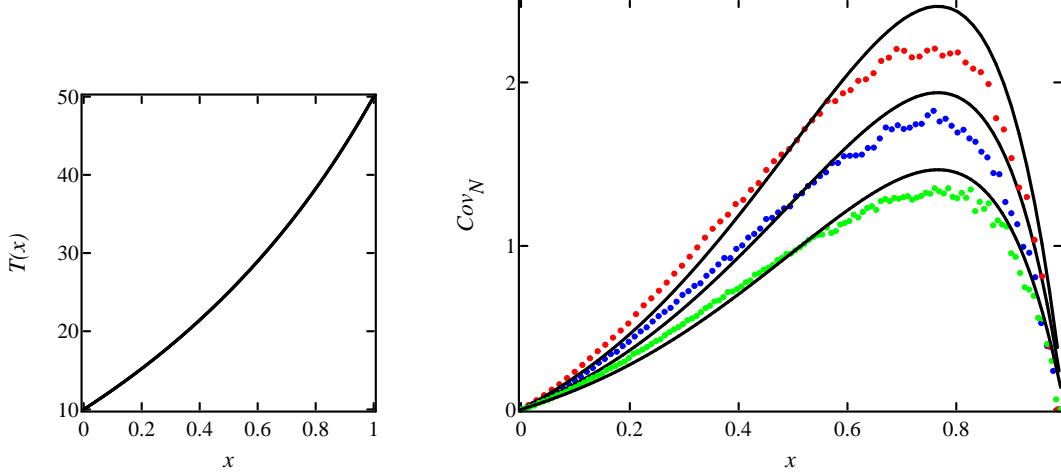
6.1 Renormalizability and the function $\mathcal{C}_2(x, y)$

In Sect. 3, we introduced the idea of a pair-covariance function $\mathcal{C}_2(x, y)$. The existence of the limit in the definition of $\mathcal{C}_2(x, y)$ implies the following: for all sufficiently large N, N' ,

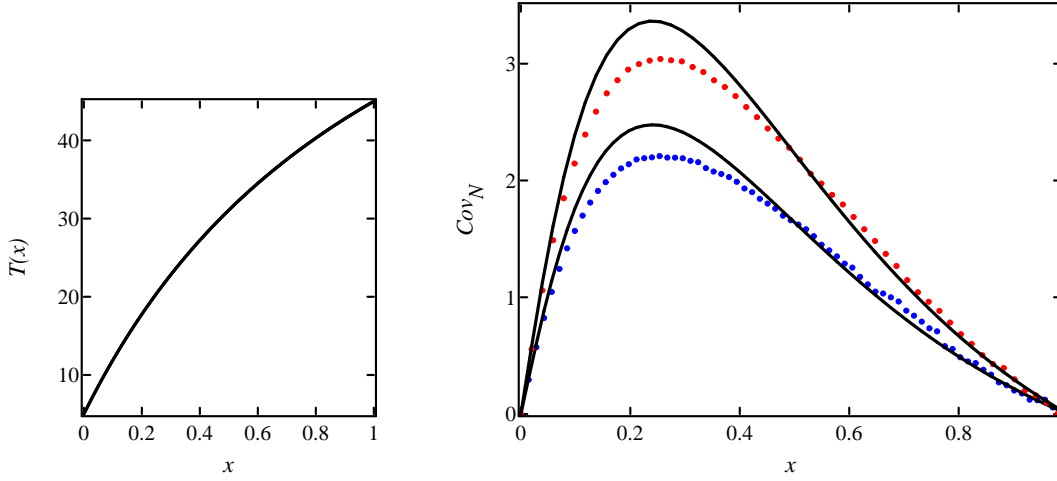
$$N \cdot \text{Cov}_N(S_{[xN]}, S_{[yN]}) \approx N' \cdot \text{Cov}_{N'}(S_{[xN']}, S_{[yN']}) . \quad (25)$$

This can be seen as a statement about the *renormalizability* of pair covariances: Consider an N -chain with $N = rN_0$ for some integers N_0 and r , and subdivide the chain into N_0 groups of r

³In Fig. 11(a), both T'^2 and A increase from left to right; in (b) T'^2 increases from 4×10^2 to 6×10^3 while A decreases from 0.07 to 0.04.



(a) $T_L = 10, T_R = 50, \rho_L = 15, \rho_R = 9; N = 70, 90, 120$



(b) $T_L = 5, T_R = 45, \rho_L = 8, \rho_R = 15; N = 50, 70$

Figure 11: Nearest-neighbor covariances. **Left column:** Temperature profiles $T(x)$. **Right column:** Empirically computed values of $\text{Cov}_N(S_i, S_{i+1})$, plotted against predicted covariances using Eq. (24). The predicted covariance curves are scaled to coincide with the empirical curves at $x = \frac{1}{2}$.

consecutive sites. For convenience, we take r to be odd. Let $i^{(r)} = (i-1)N_0 + \frac{1}{2}(r+1)$, *i.e.*, $i^{(r)}$ is the index of the middle of the r sites in the i th group. For any i, j with $1 \leq i, j \leq N_0$ and $i \neq j$, we compare the covariance at sites i and j in an N_0 -chain to that at sites $i^{(r)}$ and $j^{(r)}$ in an N -chain with the same boundary conditions. Eq. (25) tells us that $r \cdot \text{Cov}_{rN_0}(S_{i^{(r)}}, S_{j^{(r)}}) \approx \text{Cov}_{N_0}(S_i, S_j)$ if N_0 is sufficiently large, and that as $r \rightarrow \infty$, $r \cdot \text{Cov}_{rN_0}(S_{i^{(r)}}, S_{j^{(r)}})$ converges to a constant.

We test this renormalizability to confirm that $\mathcal{C}_2(x, y)$ is well defined.

Simulation 12. Fix T_L, T_R, ρ_L, ρ_R , and $N_0 \in \mathbb{Z}^+$. For various pairs (i, j) in the N_0 -chain, compute $N \cdot \text{Cov}_N(S_{i^{(r)}}, S_{j^{(r)}})$ for $N = rN_0, r = 3, 5, 7, \dots$.

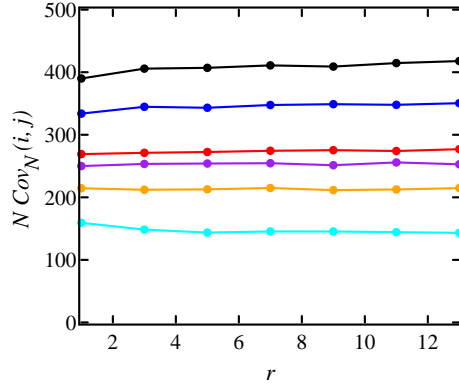


Figure 12: Renormalizability of the covariance function. The plot shows $N \cdot \text{Cov}_N(S_{i(r)}, S_{j(r)})$, where $N = rN_0$, $N_0 = 8$, and $r = 1, 3, 5, \dots, 13$. From top to bottom, the curves correspond to the (i, j) pairs $(3, 4)$, $(3, 5)$, $(2, 3)$, $(2, 4)$, $(2, 5)$, and $(2, 6)$. Boundary conditions are $T_L = 10, T_R = 100, \rho_L = 20, \rho_R = 10$.

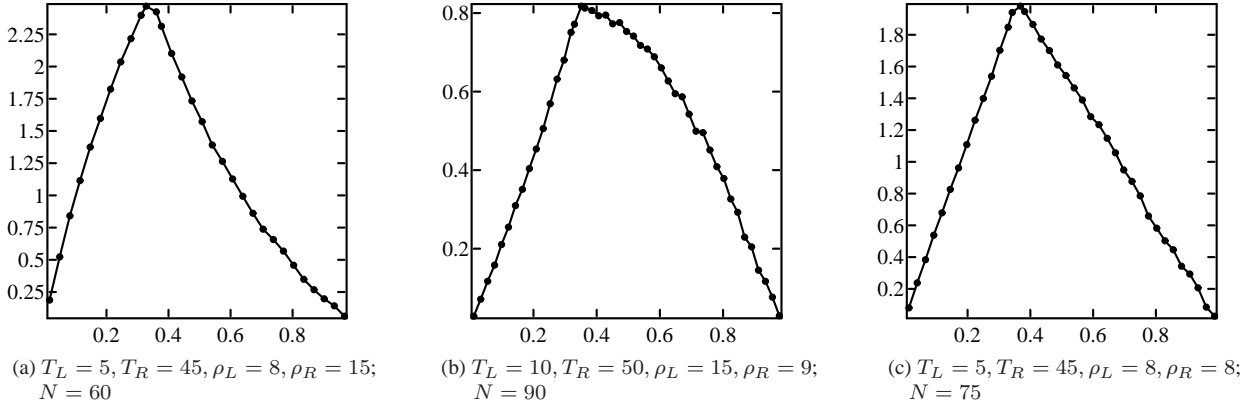


Figure 13: Covariances at macroscopic distances. These plots show $\text{Cov}_N(S_{[xN]}, S_{[yN]})$ as a function of y , with x fixed at $\approx 1/3$.

A subset of the data is shown in Fig. 12. Because the value of N_0 used is relatively small ($N_0 = 8$), one can expect the plotted values $rN_0 \cdot \text{Cov}_N(S_{i(r)}, S_{j(r)})$ to converge or stabilize to constants only as r increases. The results show that they, in fact, stabilize fairly quickly.

That $\mathcal{C}_2(x, y)$ is well defined implies that the function $(x, y) \mapsto \text{Cov}_N(S_{[xN]}, S_{[yN]})$, when normalized, settles down to a fixed shape for large N . We now investigate the shapes of these functions. While carrying out Simulations 8 and 12, we also collected data for $\text{Cov}_N(S_i, S_j)$ for various pairs of i, j . Graphs of $j \mapsto N \cdot \text{Cov}_N(S_i, S_j)$ with $i = \lfloor \frac{1}{3}N \rfloor$ are shown in Fig. 13 for three sets of boundary conditions. As predicted in Sect. 2.2, these functions are bounded, and they decrease monotonically to 0 as $|i - j|$ increases. This decay rate is roughly linear in macroscopic distance, and extraordinarily slow per lattice site. For example, if $N = 10^6$ and $i = \lfloor \frac{1}{3}N \rfloor$, then $\text{Cov}_N(S_i, S_{i+1}) \approx 2 \cdot \text{Cov}_N(S_i, S_{2i})$. We note that these findings are consistent with fluctuating hydrodynamics; see *e.g.*, [20].

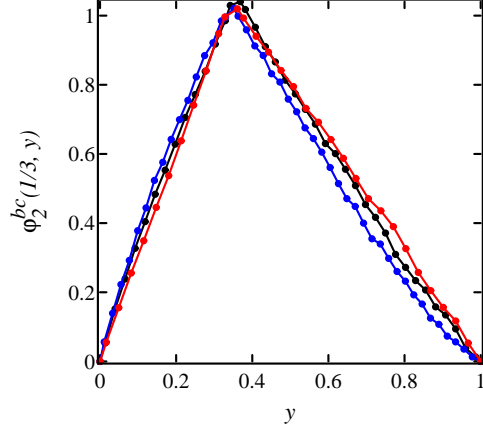


Figure 14: A slice of the 2-point distance function φ_2^{bc} . Here, we use Eqs. (26) and (27) to compute the graphs of $y \mapsto \varphi_2^{bc}(x, y)$, $x \approx \frac{1}{3}$, from the data in Fig. 13. The results are normalized to 1 at x and overlaid.

6.2 An approximate formula

A natural generalization of the nearest-neighbor covariance formula (24) to pair covariances separated by macroscopic distances is

$$\text{COV}_N(S_{[xN]}, S_{[yN]}) \approx \frac{1}{N} \cdot \varphi_2^{bc}(x, y) \cdot \bar{A}(x, y) \cdot \bar{T}'(x, y)^2. \quad (26)$$

We think of this as an approximate formula that holds for $x, y \in (0, 1)$ with $0 < |x - y| \ll 1$: $\varphi_2^{bc}(x, y)$ is a notion of effective distance of *the pair* x, y to the boundary, and \bar{A} and \bar{T}' are generalizations of corresponding quantities in (24). As a rough approximation, one may take

$$\bar{A}(x, y) = \frac{1}{2}(A(\kappa(x)) + A(\kappa(y))), \quad \bar{T}'(x, y) = \frac{T(y) - T(x)}{y - x}. \quad (27)$$

To obtain information on $\varphi_2^{bc}(x, y)$, we estimate it using (26), taking \bar{A} and \bar{T}' as above. Slices of the graphs of these functions of 2 variables, with x fixed and y varying, are shown in Fig. 14.

Piecing together these slices, we deduce the following geometric facts about our 2-point distance function φ_2^{bc} defined for $(x, y) \in (0, 1) \times (0, 1)$: it is continuous and piecewise smooth, with a “ridge” along the line $\{x = y\}$. Along that line, it is equal to $\varphi^{bc}(x) = \varphi^{bc}(y)$, the value of the 1-point distance function introduced in Sect. 4.3. For fixed x , the function $y \mapsto \varphi_2^{bc}(x, y)$ is roughly piecewise linear, peaking at $y = x$.

Observe that if this function were *exactly* piecewise linear, then by exchanging x and y , we would arrive at the relation

$$\varphi^{bc}(x) \cdot \frac{1 - y}{1 - x} = \varphi^{bc}(y) \cdot \frac{x}{y} \quad \text{for } x < y.$$

This relation implies that $\varphi^{bc}(x) = cx(1 - x)$ for some constant c . Since φ^{bc} is roughly parabolic (see Sects. 4.3 and 5.3), the approximate piecewise linearity of φ_2^{bc} is consistent with our results from previous sections. (Exact formulas for the simple exclusion [7, 20] and KMP models [3] also

contain piecewise linear functions.) On the other hand, we know from Sections 4 and 5 that for the random halves model, $\varphi^{bc}(x) \neq cx(1-x)$. Thus φ_2^{bc} cannot be exactly piecewise linear either.

In summary, our results for long-range covariances are rough and are obtained by extrapolating from what we know about covariances at microscopic distances, together with a numerical determination of the distance function φ_2^{bc} . An approximate formula is

$$\text{Cov}_N(S_{[xN]}, S_{[yN]}) \approx \begin{cases} \frac{1}{N} \cdot \left(\frac{1-y}{1-x}\right) \cdot \hat{\varphi}^{bc}(x) \cdot \bar{A}(x, y) \left(\frac{T(y)-T(x)}{y-x}\right)^2 & \text{for } 0 \leq x \leq y \leq 1, \\ \frac{1}{N} \cdot \left(\frac{y}{x}\right) \cdot \hat{\varphi}^{bc}(x) \cdot \bar{A}(x, y) \left(\frac{T(y)-T(x)}{y-x}\right)^2 & \text{for } 0 \leq y \leq x \leq 1, \end{cases}$$

where $\hat{\varphi}^{bc}$ is our approximate one-point distance function and \bar{A} is as in (27). Both this formula and Fig. 13 show clearly the following:

- (i) Covariance decays essentially linearly with macroscopic distance, *i.e.*,

$$\mathcal{C}(x) - \mathcal{C}_2(x, y) \sim |x - y|.$$

- (ii) For fixed x , the function $y \mapsto \mathcal{C}_2(x, y)$ is continuous but not differentiable at $y = x$; it has opposite concavity on the two sides of x if the temperature profile $T(y)$ is nonlinear.

That the curvature changes sign at x is clearly visible in Fig. 13; it is also evident from the second derivative of $\left(\frac{T(y)-T(x)}{y-x}\right)^2$ (see Fig. 11, left column, for the temperature profiles $T(y)$).

Conclusions and Remarks

Via a series of theoretical arguments and numerical simulations, we have developed a coherent picture for the spatial covariances at steady state of the 1-D random halves model. We have established firmly that stored-energy covariances have order of magnitude $\frac{1}{N}$ away from the boundaries of N -chains. This in itself points to the presence of long-range covariances which decay very slowly. Subsequent analysis shows that covariances decay *linearly* with macroscopic distance. For sites separated by microscopic distances, we have a simple formula that encapsulates the main ingredients on which energy covariances depend, including (i) a quadratic response to local temperature gradient, (ii) diffusive nature of the randomizing effect of the heat baths, and (iii) stabilizing effects of large numbers of tracers.

Since the random halves models are stochastic idealizations of certain mechanical models, we hope our results will also shed light on these and similar Hamiltonian systems. There are, however, important differences, such as mixing and memory issues (see *e.g.* [9, 8]). The extent to which the picture established here carries over to the Hamiltonian setting remains to be seen.

Finally, it is well known that nonequilibrium phenomena are quite different in higher dimensions. Our detailed study here provides a baseline for explorations in 2-D and 3-D, a project currently being carried out by the authors. The results, which are indeed different as predicted by fluctuating hydrodynamics, will be reported in a forthcoming paper.

Acknowledgements.

We are grateful to Jonathan Goodman, Leo Kadanoff, Oscar Lanford, Joel Lebowitz, Charles Newman, Luc Rey-Bellet and David Ruelle for helpful conversations.

Appendices

A Remarks on simulations

The simulations carried out in this paper implement directly the dynamics described in Sect. 1.1; expectation values with respect to the invariant measures are computed via time averages over long trajectories. The numerical issues are quite similar to those of Markov chain Monte Carlo computations.

We calculate empirical error bars using a standard “batch means” estimator. These error bars measure only statistical errors that arise from the fact that expectation values are estimated by time-averaging over finite intervals of time, *i.e.* finite-length trajectories. The error bars do not account for *finite-size effects*, *i.e.* bias due to the fact that we can only simulate N -chains with finite N . To improve clarity and readability, we have suppressed the error bars in most of the figures, displaying only those that are directly relevant to the issues being discussed.

A variety of variance reduction techniques have been invented to speed up the convergence of Monte Carlo calculations, ranging from multigrid Monte Carlo [19] to large deviations-based importance sampling [4]. Most of these techniques require additional information, such as an explicit expression for the invariant measure or a large deviations functional. Such methods do not work in our setting. There is on-going work on a class of algorithms which do not require detailed knowledge of the invariant measure [12]. However, it is not known whether such techniques can be applied to the random halves model.

The quantities of interest in most of our simulations are the $\text{Cov}_N(S_i, S_j)$. In general, these are relatively small numbers that are differences of two much larger numbers and can be rather costly to compute. We estimate the cost of computing Cov_N as follows: for temperatures which are $\sim T$, both $\mathbb{E}(S_i S_j)$ and $\mathbb{E}(S_i)\mathbb{E}(S_j)$ are $\sim T^2$, while $\text{Cov}_N(S_i, S_j) \sim A(\bar{\kappa})T'^2/N$, where $\bar{\kappa}$ is the typical tracer density per site. (For the present discussion, we focus on i, j away from the boundaries so that $\varphi^{bc}(x) \sim 1$.) In order to compute $\text{Cov}_N(S_i, S_j)$ with a relative error of ε , we need $\mathbb{E}(S_i S_j)$ with a relative error of $\varepsilon A(\bar{\kappa})(T'/T)^2/N$; the same is true for $\mathbb{E}(S_i)\mathbb{E}(S_j)$. Since the statistical error in the time average $\frac{1}{\tau} \int_0^\tau S_i(\tau') S_j(\tau') d\tau'$ is $\sim \sqrt{\alpha/\tau}$ for some α , this means we need to integrate the system for a time τ which is proportional to $N^2/\varepsilon^2 A(\bar{\kappa})^2 \cdot (T/T')^4$. Now, the computational cost of simulating the system up to time τ , as measured by the total number of “events,” is proportional to the number of tracers $\bar{\kappa}N$ in the system and the mean rate of activity of each tracer (which is $\sim \sqrt{T}$). Thus, we have

$$\text{computational cost} \sim \alpha \cdot \frac{N^3 \bar{\kappa}}{\varepsilon^2 A(\bar{\kappa})^2} \left(\frac{T}{T'} \right)^4 \sqrt{T}. \quad (28)$$

For our simulations involving long chains, we have found α to be typically $\lesssim 10$. As an example, for $\varepsilon = 5\%$, $N = 60$, $T_L = 5$, $T_R = 45$, $\rho_L = \rho_R = 8$, we have $\bar{\kappa} \approx 6$, and $A(\bar{\kappa}) \sim 0.1$, so that

$\sim 4 \times 10^{11}$ events are needed. On our computer system,⁴ this requires ~ 14 days.

Eq. (28) tells us that the computational cost grows rapidly as T'/T decreases. In Simulations 4, 6, and 9, where we study the small- T' behavior of the covariance function, this rapid growth prevents us from taking T' too small. However, we do not always need small T'/T , and a large temperature gradient not only reduces the computational cost, it also takes the system farther out of equilibrium so that some effects are made more transparent.

The cost also grows rapidly as N increases. This is why we use short chains wherever possible, for example in computing the A -curve. In Simulation 5, we use $N = 8$ because we feel that the amount of accuracy gained from using longer chains is perhaps not worth the additional cost. However, it is not always possible or advisable to use short chains, particularly where infinite-volume limits are involved. In such cases, one can sometimes obtain better results by increasing T'/T .

Finally, recall that $A(\bar{\kappa}) \sim 1/\bar{\kappa}$ for $\bar{\kappa} \gg 1$, so the computational cost is $\sim \bar{\kappa}^3$ for large $\bar{\kappa}$.

B Invariant measures

Proof of Proposition 5.1: The proof of invariance of the measure $\mu^{T,\rho_1} \times \dots \times \mu^{T,\rho_N}$ follows closely that of Proposition 3.7 in [9]. We refer the reader to [9] for some of the background notation. Fix a phase point

$$\bar{z} = (\bar{z}^{(1)}, \dots, \bar{z}^{(N)}) = (\{\bar{x}_1^{(1)}, \dots, \bar{x}_{k_1}^{(1)}\}, y^{(1)}; \dots; \{\bar{x}_1^{(N)}, \dots, \bar{x}_{k_N}^{(N)}\}, y^{(N)}).$$

We assume $\bar{x}_1^{(n)}, \dots, \bar{x}_{k_n}^{(n)}$ are distinct, and let $\varepsilon, h > 0$ be arbitrarily small numbers. Fix arbitrary n with $1 < n < N$. We will compare the 3 probabilities, $P_{n,\cdot}$, $P_{n+1,n}$ and $P_{n-1,n}$ defined below:

Let $P_{n,\cdot}$ be the probability that at time $t = 0$, in every site j , there are exactly k_j tracers the energies of which lie in disjoint intervals

$$[\bar{x}_1^{(j)}, \bar{x}_1^{(j)} + \varepsilon], \quad \dots, \quad [\bar{x}_{k_j}^{(j)}, \bar{x}_{k_j}^{(j)} + \varepsilon],$$

and before $t = h$, the tracer in site n with energy in $[\bar{x}_1^{(n)}, \bar{x}_1^{(n)} + \varepsilon]$ exits the site. The number $P_{n+1,n}$ is the probability that at time 0, the tracer configuration is as above except that the tracer with energy in $[\bar{x}_1^{(n)}, \bar{x}_1^{(n)} + \varepsilon]$ is in site $n + 1$ instead of site n (i.e., there are $k_n - 1$ tracers in site n and $k_{n+1} + 1$ tracers in site $n + 1$), and before time $t = h$, this tracer jumps from site $n + 1$ to site n . The number $P_{n-1,n}$ is defined analogously with site $n - 1$ playing the role of site $n + 1$.

To prove the invariance of $\mu^{T,\rho_1} \times \dots \times \mu^{T,\rho_N}$, three sets of balancing conditions have to be met. The interaction with tanks is as in [EY]. We verify below the equation involving interaction between neighbors, namely $P_{n,\cdot} = P_{n+1,n} + P_{n-1,n}$, and leave the one involving interaction with a bath to the reader.

⁴We performed most of our simulations using GCC on 900 MHz SPARCv9 processors. Note that this running time estimate also depends on how much information is collected during the simulation.

Let σ_k, c_k and p_k be as in Proposition 1.1 (Sect. 1.2). We will use the shorthand $\sigma_{k_i} = \sigma_{k_i}(\bar{z}^{(i)})$, and write $p_k^{(i)}$ to remind ourselves that $\rho = \rho_i$ at site i (c_k and σ_k do not depend on ρ). First,

$$\begin{aligned} P_{n,\cdot} &= \prod_{i=1}^N p_{k_i}^{(i)} c_{k_i} \sigma_{k_i} \varepsilon^{k_i+1} \cdot \sqrt{\bar{x}_1^{(n)}} e^{\beta \bar{x}_1^{(n)}} \frac{1}{\varepsilon} \cdot \int_{\bar{x}_1^{(n)}}^{\bar{x}_1^{(n)}+\varepsilon} h \sqrt{x} \frac{1}{\sqrt{x}} e^{-\beta x} dx \\ &= h \cdot \prod_{i=1}^N p_{k_i}^{(i)} c_{k_i} \sigma_{k_i} \varepsilon^{k_i+1} \sqrt{\bar{x}_1^{(n)}} := h \cdot Z \end{aligned}$$

where Z is defined by the equality above. Next, $P_{n+1,n} = \frac{1}{2} I \cdot II \cdot III$ where

$$\begin{aligned} I &= \prod_{i \neq n, n+1} (p_{k_i}^{(i)} c_{k_i} \sigma_{k_i} \varepsilon^{k_i+1}), \\ II &= p_{k_{n-1}}^{(n)} c_{k_{n-1}} \sigma_{k_n} \sqrt{\bar{x}_1^{(n)}} e^{\beta \bar{x}_1^{(n)}} \varepsilon^{k_n}, \\ III &= p_{k_{n+1}+1}^{(n+1)} c_{k_{n+1}+1} \sigma_{k_{n+1}} \varepsilon^{k_{n+1}+1} \int_{\bar{x}_1^{(n)}}^{\bar{x}_1^{(n)}+\varepsilon} h \sqrt{x} \frac{1}{\sqrt{x}} e^{-\beta x} dx. \end{aligned}$$

This product can be written as

$$\frac{h}{2} \cdot Z \cdot \left(\frac{p_{k_{n-1}}^{(n)} c_{k_{n-1}}}{p_{k_n}^{(n)} c_{k_n}} \right) \cdot \left(\frac{p_{k_{n+1}+1}^{(n+1)} c_{k_{n+1}+1}}{p_{k_{n+1}}^{(n+1)} c_{k_{n+1}}} \right) = \frac{h}{2} \cdot Z \cdot \left(\frac{T}{2\rho_n} \right) \cdot \left(\frac{2\rho_{n+1}}{T} \right).$$

The equality above follows from the relation

$$\frac{c_k p_k}{c_{k+1} p_{k+1}} = \frac{T}{2\rho},$$

which can be derived from the characterization of $\mu^{T,\rho}$ (Proposition 1.1). An analogous argument holds for $P_{n-1,n}$, and the desired equality follows from

$$\frac{1}{2} \left(\frac{\rho_{n+1}}{\rho_n} + \frac{\rho_{n-1}}{\rho_n} \right) = 1.$$

□

References

- [1] L. Bertini, A. De Sole, D. Gabrielli, G. Jona-Lasinio, C. Landim, “Fluctuations in stationary nonequilibrium states of irreversible processes,” *Phys. Rev. Lett.* **87** (2001) 040601-1
- [2] L. Bertini, A. De Sole, D. Gabrielli, G. Jona-Lasinio, C. Landim, “Macroscopic fluctuation theory for stationary non-equilibrium states,” *J. Statist. Phys.* **107** (2002) pp. 635–675
- [3] L. Bertini, D. Gabrielli, J. L. Lebowitz, “Large deviations for a stochastic model of heat flow,” *J. Stat. Phys.* **121** (2005) pp. 843–885

- [4] J. A. Bucklew, *Introduction to Rare Event Simulation*, Springer-Verlag (2004)
- [5] S. R. de Groot, P. Mazur, *Non-equilibrium Thermodynamics*, North-Holland (1962)
- [6] B. Derrida, “An exactly soluble non-equilibrium system: the asymmetric simple exclusion process,” *Phys. Rep.* **301** (1998) pp. 65–83
- [7] B. Derrida, J. L. Lebowitz, E. R. Speer, “Large deviation of the density profile in the steady state of the open symmetric simple exclusion process,” *J. Statist. Phys.* **107** (2002) pp. 599–634
- [8] J.-P. Eckmann, C. Mejía-Monasterio, E. Zabey, “Memory effects in nonequilibrium transport for deterministic Hamiltonian systems,” to appear in *J. Stat. Phys.* (2006)
- [9] J.-P. Eckmann, L.-S. Young, “Nonequilibrium energy profiles for a class of 1-D models,” *Comm. Math. Phys.* **262** (2006) pp. 237–267
- [10] D. Forster, *Hydrodynamic Fluctuations, Broken Symmetry, and Correlation Functions*, Addison-Wesley (1990)
- [11] P. L. Garrido, J. L. Lebowitz, C. Maes, H. Spohn, “Long-range correlations for conservative dynamics,” *Phys. Rev. A* **42** (1990) pp. 1954–1968
- [12] J. B. Goodman, K. K. Lin, “Coupling and control variates in dynamic Monte Carlo,” in preparation
- [13] C. Kipnis, C. Marchioro, E. Presutti, “Heat flow in an exactly solvable model,” *J. Stat. Phys.* **27** (1982) pp. 65–74
- [14] C. Kipnis, C. Landim, *Scaling Limits of Interacting Particle Systems*, Berlin: Springer-Verlag (1999)
- [15] T. R. Kirkpatrick, E. G. D. Cohen, J. R. Dorfman, “Fluctuations in a nonequilibrium steady state: basic equations,” *Phys. Rev. A* **26** (1982) pp. 950–971
- [16] H. Larralde, F. Leyvraz, C. Mejía-Monasterio, “Transport properties of a modified Lorentz gas,” *J. Stat. Phys.* **113** (2003) pp. 197–231
- [17] S. Lepri, R. Livi, and A. Politi, “Thermal conduction in classical low-dimensional lattices,” *Physics Reports* **377** (2003)
- [18] C. Mejía-Monasterio, H. Larralde, F. Leyvraz, “Coupled normal heat and matter transport in a simple model system,” *Phys. Rev. Lett.* **86** (2001) pp. 5417–5420
- [19] A. D. Sokal, “Monte Carlo methods in statistical mechanics: foundations and new algorithms,” in *Functional Integration: Basics and Applications*, NATO Adv. Sci. Inst. Ser. B Phys. **361** (1997)

- [20] H. Spohn, “Long range correlations for stochastic lattice gases in a nonequilibrium steady state,” *J. Phys. A* **16** (1983) *pp.* 4275–4291